This is a repository copy of *Measurement of magnetic cavitation driven by heat flow in a plasma*.

White Rose Research Online URL for this paper:
https://eprints.whiterose.ac.uk/200261/

Version: Published Version

Article:

Arran, Christopher orcid.org/0000-0002-8644-8118, Dearling, Adam, Bradford, Philip et al. (13 more authors) (2023) Measurement of magnetic cavitation driven by heat flow in a plasma. Physical Review Letters. 015101. ISSN 1079-7114

https://doi.org/10.1103/PhysRevLett.131.015101

Reuse

This article is distributed under the terms of the Creative Commons Attribution (CC BY) licence. This licence allows you to distribute, remix, tweak, and build upon the work, even commercially, as long as you credit the authors for the original work. More information and the full terms of the licence here: https://creativecommons.org/licenses/

Takedown

If you consider content in White Rose Research Online to be in breach of UK law, please notify us by emailing eprints@whiterose.ac.uk including the URL of the record and the reason for the withdrawal request.

eprints@whiterose.ac.uk
https://eprints.whiterose.ac.uk/

Measurement of Magnetic Cavitation Driven by Heat Flow in a Plasma

C. Arran,[1,*] P. Bradford,[1,†] A. Dearling,[1] G. S. Hicks,[2] S. Al-Atabi,[2] L. Antonelli,[3] O. C. Ettlinger,[2]
M. Khan,[1] M. P. Read,[3] K. Glize,[4,‡] M. Notley,[4] C. A. Walsh,[5] R. J. Kingham,[6]
Z. Najmudin,[2] C. P. Ridgers,[1] and N. C. Woolsey[1]
[1]*York Plasma Institute, University of York, York YO10 5DD, United Kingdom*
[2]*The John Adams Institute for Accelerator Science, Blackett Laboratory, Imperial College London, London SW7 2BZ, United Kingdom*
[3]*First Light Fusion Ltd., Unit 9/10 Oxford Industrial Park, Mead Road, Yarnton, Kidlington OX5 1QU, United Kingdom*
[4]*Central Laser Facility, STFC Rutherford Appleton Laboratory, Harwell Campus, Didcot OX11 0QX, United Kingdom*
[5]*Lawrence Livermore National Laboratory, 7000 East Avenue, Livermore, California 94550-9234, USA*
[6]*Blackett Laboratory, Imperial College London, London SW7 2BZ, United Kingdom*

(Received 20 May 2022; revised 22 March 2023; accepted 17 May 2023; published 6 July 2023)

We describe the direct measurement of the expulsion of a magnetic field from a plasma driven by heat flow. Using a laser to heat a column of gas within an applied magnetic field, we isolate Nernst advection and show how it changes the field over a nanosecond timescale. Reconstruction of the magnetic field map from proton radiographs demonstrates that the field is advected by heat flow in advance of the plasma expansion with a velocity $v_N = (6 \pm 2) \times 10^5$ m/s. Kinetic and extended magnetohydrodynamic simulations agree well in this regime due to the buildup of a magnetic transport barrier.

DOI: 10.1103/PhysRevLett.131.015101

In extreme pressures and temperature gradients, heat flow and magnetic fields are strongly coupled, but although theoretical work shows that strong heat flows can cause significant changes in the magnetic field [1–3], it has long proven difficult to measure these changes experimentally. A particular challenge in magnetized plasma experiments is Nernst-driven magnetic cavitation, in which heat flow causes expulsion of the magnetic field from the hottest regions of a plasma. This reduces the effectiveness of magnetized fusion techniques [4,5], where strong magnetic fields are employed to confine the heat inside the plasma and increase yield [6–9].

The Nernst effect is familiar in semiconductors and has been measured in semimetals and even superconductors [10]. In all of these cases, mobile charge carriers in a temperature gradient are deflected by a perpendicular magnetic field. The larger gyroradii and lower collision frequency of particles at higher temperatures results in net momentum of carriers perpendicular to both the temperature gradient and the magnetic field, establishing an electric field. In plasmas, this is typically described using classical transport theory by the thermal force acting on electrons as $\mathbf{F}_\perp \propto -\nabla T_e \times \mathbf{B}$ [2]. When the Nernst electric field has a nonzero curl, the net motion of charge carriers drives advection of the magnetic field as $\partial \mathbf{B}/\partial t = \nabla \times (\mathbf{v_N} \times \mathbf{B})$, where the Nernst advection velocity is given by $\mathbf{v_N} \approx 2\boldsymbol{\phi}_\mathbf{q}/5n_eT_e$ for a heat flow $\boldsymbol{\phi}_\mathbf{q}$ [3,11]. That is, the magnetic field is transported down temperature gradients by heat flow as well as being transported down pressure gradients by bulk plasma flow. This Nernst advection causes expulsion of the magnetic field from a hot plasma without a corresponding change in the plasma density profile, a result which cannot be explained by common models using purely ideal or resistive magnetohydrodynamics (MHD).

In general, Nernst advection is the dominant means of magnetic field transport wherever the speed of the heat flow is faster than both the bulk motion and the rate of magnetic dissipation; previous experiments which measured the Biermann battery in laser-solid interactions have shown that models of magnetized plasmas which neglect the Nernst effect fail during fast heating processes [12–16]. Furthermore, because heat flow depends on higher order moments of the velocity distribution, a Maxwellian approximation for heat flow is less accurate than for plasma density or current. As temperature gradients become steeper, even extended MHD (XMHD) models for Nernst advection will fail. Under these nonlocal conditions, when the electron mean free path is no longer small compared to the length scale of the temperature gradient, neither the heat flow nor the Nernst velocity are proportional to the local electron temperature gradient. While the effect of nonlocality and magnetic fields upon the temperature profile has been explored before [17–19], nonlocal changes to the magnetic field have so far only been studied in kinetic simulations using Vlasov-Fokker-Planck (VFP) codes, which include

---

Published by the American Physical Society under the terms of the Creative Commons Attribution 4.0 International license. Further distribution of this work must maintain attribution to the author(s) and the published article's title, journal citation, and DOI.

the Nernst effect implicitly [20,21]. Nernst advection therefore makes an excellent laboratory to measure kinetic effects, where changes to the heat dynamics directly affect the magnetic field.

We describe a laser-plasma experiment to measure the effect of heat flow on an applied magnetic field. Using laser-driven proton radiography [22] of an applied magnetic field, we demonstrate that Nernst advection dominates changes to the magnetic field in underdense plasmas on nanosecond timescales. Unlike previous experiments, we isolate Nernst advection and show that the magnetic field dynamics are decoupled from motion of the plasma.

We focused a 1.5 ns duration heater beam through a nitrogen gas target, propagating antiparallel to the 3 T applied field as shown in Fig. 1. Laser intensities of 10^{16} W cm^{-2} were reached in a spot size of 19 μm FWHM over a Rayleigh length of ≈1 mm. This produced an approximately cylindrically symmetric plasma with electron densities of 10^{18}–10^{19} cm^{-3} over a scale length of ∼100 μm, with a temperature of around 700 ± 300 eV at the highest electron density, as estimated from the measured thermoelectric field (see Supplemental Material [23] for details). This gives a ratio between the cyclotron frequency ω_c and the collision frequency $1/\tau_e$ described by a Hall parameter around $\omega_c \tau_e \approx 1 - 10$. Under these conditions, the magnetic field and heat flow are strongly coupled, with the magnetic field restricting perpendicular heat flow, but heat flow also affecting the magnetic field dynamics. The changes in the magnetic field are described by [32]:

$$\frac{\partial \mathbf{B}}{\partial t} = \boldsymbol{\nabla} \times (\mathbf{v}_{\mathbf{B}} \times \mathbf{B}) + \boldsymbol{\nabla} \times \left(\frac{1}{\mu_0 \sigma_\perp} \boldsymbol{\nabla} \times \mathbf{B} \right) + \frac{\boldsymbol{\nabla} T_e \times \boldsymbol{\nabla} n_e}{e n_e}, \tag{1}$$

where the first term describing advection is a combination of the hydrodynamic motion and the Nernst advection as $\mathbf{v}_{\mathbf{B}} = \mathbf{u} - (1 + \delta_\perp^c)(\mathbf{J}/e n_e) + \mathbf{v}_{\mathbf{N}}$, where under our magnetized conditions the Braginskii coefficient $\delta_\perp^c \sim 0.1$. This gives $\mathbf{v}_{\mathbf{B}} \approx \mathbf{v}_{\mathbf{e}} + \mathbf{v}_{\mathbf{N}}$ [32], for electron motion $\mathbf{v}_{\mathbf{e}}$. We estimate a sound speed on the scale of 10^5 m/s and a thermal diffusivity on the order of 10^4 m^2/s, giving a thermal Péclet number of Pe $\sim 10^{-2}$. This makes heat conduction dominant over convection, indicating the importance of Nernst advection, while the Knudsen number $\lambda_{\mathrm{mfp},e}/l_T \approx 1$, showing the importance of nonlocality. The Braginskii conductivity is around $\sigma_\perp \sim 10^7$ S/m, giving a magnetic Reynolds number of Re$_M \sim 100$ and allowing us to neglect the magnetic diffusion and resistivity gradient flow described by the second term. The cylindrically symmetric geometry is chosen such that the final Biermann term for generating magnetic fields is negligible, with $\boldsymbol{\nabla} T_e \| \boldsymbol{\nabla} n_e$. Shots without an applied magnetic field showed no magnetic field generation. Under our conditions the only possible contributions to changes in the magnetic field are therefore Nernst advection and hydrodynamic advection ("frozen in flow").

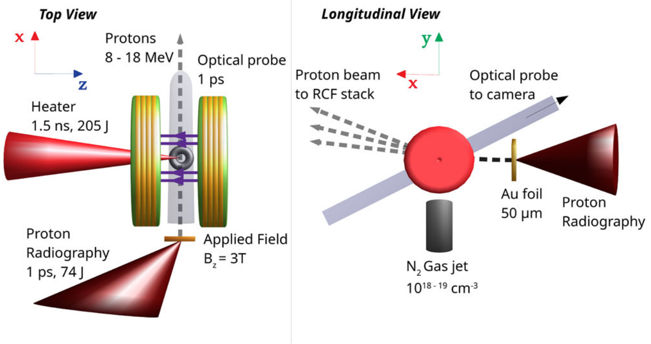

FIG. 1. Experimental layout shown from above (left) and from along the z axis (right). The 1.5 ns-duration heater beam (solid red) is focused along the z axis to a point 2 mm above the gas jet nozzle. A 1 ps-duration proton radiography beam (solid red) is focused onto a gold foil, producing a proton beam (gray dashed) which passes through the interaction point along the x axis, perpendicular to the heater beam, and is deflected upward by the applied magnetic field. The 1 ps-duration collimated optical probe beam (translucent gray) also passes through the interaction point in the x-y plane, perpendicular to the heater beam.

The hydrodynamic advection was studied using optical interferometry. The 1 ps-duration collimated probe beam passed transversely through the plasma column, with the interaction point reimaged onto an Andor Neo camera after passing through a Mach-Zehnder interferometer. The interferograms [examples shown in Fig. 2(a)(i), with further data in the Appendix] measure a plasma column much longer than it is wide, which was found to be largely symmetric by performing separate Abel inversions of the top and bottom halves of the data, before combining both halves to a symmetric map. The resulting density map and radial density profiles are shown in Figs. 2(a)(ii) and 2(a)(iii). Two laser shots were conducted under the same conditions, with the probe passing through the plasma at early and late times (0.4 and 1.1 ns).

The recovered density shown in the top panels of Figs. 2(a)(ii) and 2(a)(iii) demonstrates that 0.4 ns after the start of the heater beam, a plasma column has been formed with a diameter of around 300 μm over a length of slightly under 2 mm longitudinally, with a peak density around 10^{19} cm^{-3}. At these relatively early times, the plasma is not yet fully ionized and the plasma column shows no sign of cavitation. As the heater beam continues to ionize more gas and the plasma expands, however, a density cavity forms inside the plasma column by 1.1 ns after the start of the heater beam, shown in the bottom panels.

The magnetic field evolution was measured using proton radiography performed using a broadband target normal sheath acceleration proton source [22]. Protons were generated by focusing a 1 ps duration laser pulse onto a 50 μm thick gold foil using an $f/3$ off-axis paraboloid.

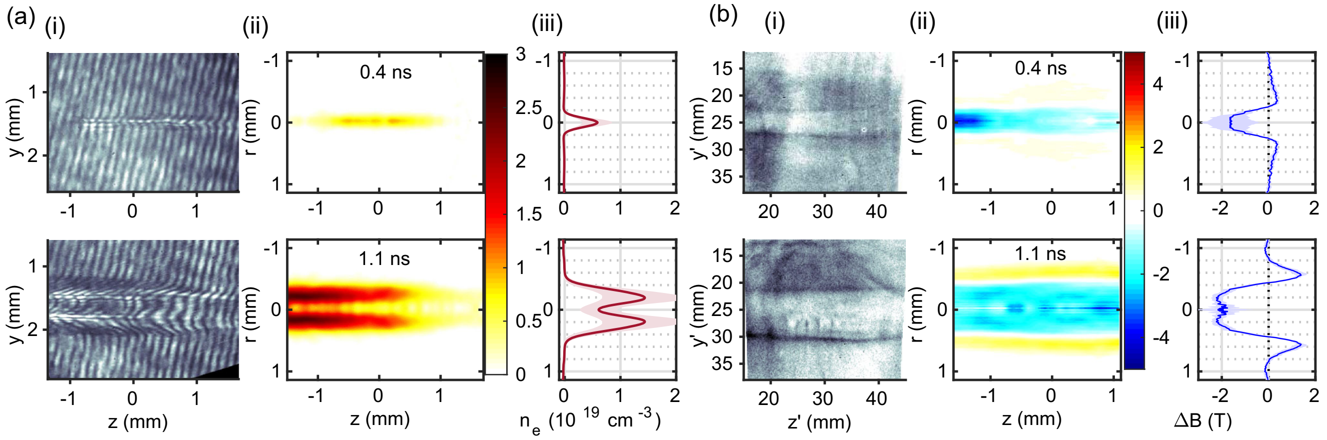

FIG. 2. (a) Interferometry results measured 0.4 ns after the start of the heater beam (top panels) and 1.1 ns after (bottom). (i) The raw interferogram measured on the camera is shown on the left, with fringe shifts showing the presence of a long plasma column. (ii) From this interferogram we reconstruct a map of the plasma density, shown as a cross section through the center of the column. (iii) The longitudinally averaged mean of the radial plasma density profile is shown to the right of this, with the shaded region showing the standard deviation longitudinally. (b) Radiography results measured at the same times. (i) The raw radiograph is shown on the left, with darker regions showing a higher proton dose. (ii) The change in the magnetic field reconstructed from the radiograph is shown as a cross section through the center of the plasma column, with (iii) the longitudinally averaged mean and standard deviation of the radial magnetic field profile to the right.

This proton beam passed from the foil, 20 mm from the interaction point, transversely through the plasma column, before being measured by a stack of Gafchromic EBT3 radiochromic film (RCF) 167 mm after the interaction point, giving a magnification of 9.35. The proton intensity distribution measured by radiographs, as shown in Fig. 2(b)(i), can therefore be used to reconstruct the magnetic fields through which the protons have passed [33,34]. Shots taken without the applied magnetic field showed that the signal from electric fields was much weaker than the signal from magnetic fields, with proton deflections below 0.1 mrad, around an order of magnitude smaller than deflections when an applied field was present.

However, the proton beam in this experiment was deflected by both the signal region within the plasma and also the constant applied magnetic field in a much larger region surrounding the plasma. This blurs out the radiographs and changes the symmetry of the signal. We therefore used a deconvolution algorithm to remove the effect of the background field, accounting for the finite energy absorption range of the RCF, the broadband proton source, and the deflection in the background field, as described in Ref. [35] (see Supplemental Material [23] for more details), with a spatial resolution of around 50 μm for 10 MeV protons. The resulting monoenergetic radiographs were largely antisymmetric, allowing us to recover the magnetic fields separately from the thermoelectric field. The recovered change in the magnetic fields is shown in Figs. 2(b)(ii) and 2(b)(iii), where on each of the two shots the proton beam was timed such that the 10.6 MeV protons most strongly absorbed in the third layer of the RCF stack passed through the plasma simultaneously with the optical probe to within the temporal resolution of tens of picoseconds.

Shortly after the start of the heater beam, at 0.4 ns, a strong reduction in the magnetic field strength by −2 T in the central region is already visible in the top panel of Fig. 2(b)(iii), despite no cavitation in the plasma density. The applied magnetic field is advected to the edge of the plasma by heat flow, resulting in an increase in the magnetic field strength further off axis, at a radius of around 350 μm. The spatial size of the cavitation is fairly uniform over a length of around 2 mm, with the field cavitated over the whole of the hot plasma. This decoupling of the magnetic field profile from the plasma flow is a clear signature of the Nernst effect; this is the first time this has been measured in experiment.

The magnetic field and density profiles at these two different times are overlaid in Fig. 3(a) for comparison. The magnetic field is advected to the sheath plasma region and within the hot plasma is reduced to less than a third of its original strength. Figure 3(a) shows that Nernst advection is significantly faster than hydrodynamic motion under these conditions. Heat flow drives cavitation in the magnetic field over a large region, before any cavitation occurs in the plasma density, with preheating reaching out to $r > 0.5$ mm. We can therefore estimate the Nernst velocity at 0.4 ns by measuring the radius of the peak magnetic field at different times, reconstructed from five different proton radiographs taken on the same shot (RCF layers 2–6, absorbing proton energies from 7.6–18.3 MeV). This gives a measured Nernst velocity at these early times of $(6 \pm 2) \times 10^5$ m/s.

The Nernst velocity gives an estimate for the heat flux as $\phi_q = 5n_eT_ev_N/2$, which can be compared to the

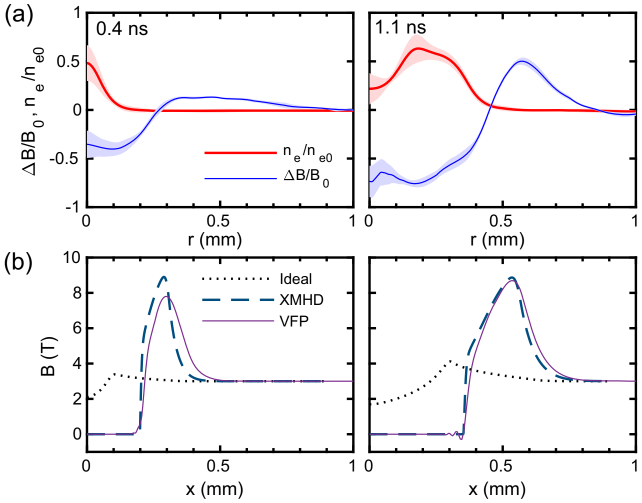

FIG. 3. (a) The reconstructed profiles of the magnetic field (blue) and density (red) against radius, measured at 0.4 ns (left panels) and 1.1 ns (right) and normalized to a background magnetic field $B_0 = 3$ T and a fully ionized density $n_{e0} = 2.4 \times 10^{19}$ cm^{-3}. Both profiles are longitudinally averaged over the central 1 mm of plasma, with the shaded area showing the standard deviation. (b) The magnetic field profile predicted from one-dimensional simulations, showing an ideal MHD model without the Nernst effect (dotted black line), an XMHD model including the thermoelectric Nernst term (dashed dark blue), and results from kinetic VFP simulations, with Nernst advection included implicitly (solid purple).

free-streaming heat flux $\phi_{\mathrm{fs}} = n_e T_e v_{\mathrm{th},e}$ for a thermal velocity $v_{\mathrm{th},e}$. Given that the electron thermal velocity at 700 eV is 1.6×10^7 m/s, we infer a heat flux at 0.4 ns at least one tenth of the free-streaming limit, showing the importance of correctly modeling the heat transport at these early times. Indeed, the Braginskii estimate for the heat flow, given the measured density and temperature profiles at 0.4 ns, reaches 300 TW/m^2. This corresponds to a predicted Nernst velocity of 4×10^5 m/s, consistent with the measured advection.

However, the Nernst velocity falls as time goes on and the heat flow reduces, with the change in peak magnetic field position between 0.4 and 1.1 ns corresponding to an average advection velocity of just $(2.7 \pm 1.0) \times 10^5$ m/s. Measuring the half width at half maximum of the density profile at 1.1 ns gives an average bulk velocity of $\approx 3 \times 10^5$ m/s, which is comparable to the ion sound speed at 700 eV. Whereas at early times magnetic field advection is dominated by hot electrons through the Nernst effect, at later times hydrodynamic motion on the timescale of ion motion becomes more important.

We model the plasma and magnetic field evolution with CTC [36]—an XMHD code which includes Nernst advection with a flux-limited model of heat flow—and a kinetic VFP code, IMPACT [37], in a 1D planar geometry, to see the effects of the Nernst term and of different treatments of heat transport. Both simulations began with a uniform fully ionized $Z = 7$ plasma at a density of $n_{e0} = 2.4 \times 10^{19}$ cm^{-3} and modeled laser heating using a realistic temporal profile. Figure 3(b) shows the predictions from IMPACT and the predictions from CTC both with and without the Nernst term. The scale of magnetic cavitation cannot be explained without invoking the Nernst effect, as ideal MHD simulations with the Nernst term turned off (shown by the black dotted line) predict only slight and slow-moving cavitation which approximately matches the density profile. Once the Nernst effect is included, however, the fluid and kinetic simulations (dashed and solid line, respectively) closely agree and both capture the shape of the magnetic field profile at later times. The long tail in the magnetic field peak at 0.4 ns implies that the plasma was heated by additional processes beyond inverse bremsstrahlung over a much larger area than the initial laser spot, but as the plasma evolves the magnetic field profile shows the formation of a steeper heat front.

That the fluid and kinetic simulations agree so closely is surprising, as both simulations predict mean free paths on the order of 100 μm, where the fluid model should break down. In the one-dimensional simulations shown here, however, the increase in the magnetic field at the edge of the hot plasma means the Hall parameter at the heat front reaches $\omega_c \tau_e \approx 10$ by 1.1 ns. In this regime the heat transport becomes limited by the electron gyroradius rather than by the mean free path, with the Nernst growth rate described by Sherlock and Bissell [38] changing from $\tilde{N}\tau_{ei} \sim (\lambda_{\mathrm{mfp},e}/l_T)^2 \approx 1$ to $\tilde{N}\tau_{ei} \sim (r_c/l_T)^2 \lesssim 0.1$. At early times the kinetic and fluid simulations predict different heat flows, but at later times the Nernst effect increasingly leads to a magnetic transport barrier which keeps the heat flow in a relatively local regime, even as the magnetic field inside the cavity falls to zero.

To further explore this effect, laser shots were taken at three different gas jet backing pressures. The resulting magnetic field profiles are shown in Fig. 4(a), measured

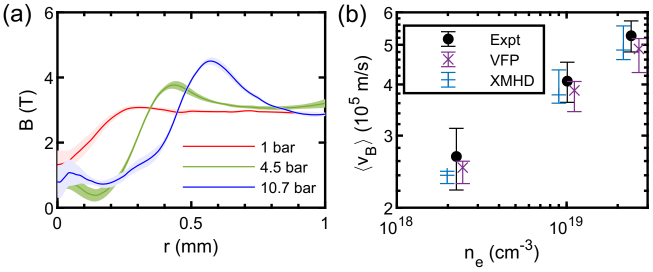

FIG. 4. (a) The recovered magnetic field profiles measured 1.1 ns after the arrival of the heater beam for three different backing pressures, showing the mean and standard deviation of the magnetic field over a 1 mm long section in the middle of the gas jet. (b) Comparing results from the simulations and the experiments, the average advection velocity of the magnetic field in the time up to 1.1 ns is measured by the position of the peak in the magnetic field.

1.1 ns after the start of the heater beam (further data in the Appendix). At lower densities the plasma is less collisional, with a lower rate of inverse bremsstrahlung heating resulting in a colder plasma. The mean free path predicted by simulations increases to 300 μm at 1 bar while the maximum Hall parameter increases to $\omega_c \tau_e \approx 40$. This means both that the speed of heat flow is lower at lower densities—leading to slower magnetic advection and less cavitation as observed in the experiment—and also that the magnetic barrier further constrains the heat flow. In a strongly magnetized plasma we would expect the rate of heat flow to scale as $v_N \propto \tau_e^{-1} \propto n_e T_e^{-1.5}$ [32].

We estimate how the Nernst advection rates change with density by measuring the position of the peak in the magnetic field at 1.1 ns in both the experiment and 1D simulations without a flux limiter; these results are shown in Fig. 4(b). In all cases, the advection velocity falls with decreasing density, with the simulations very closely reproducing the behavior measured in experiment. Fitting the measured average advection velocities to a power law, however, gives a trend $v_B \propto n_{e0}^{0.30\pm0.03}$. Our simulations show that $v_B \propto T_e^{0.2}$ in 1D and although the collision time is a factor of 5 higher at the lowest density, the advection velocity is only reduced by a factor of 2. The stronger magnetization localizes the heat flow, but the Nernst advection is still faster than for a strongly magnetized plasma, particularly at early times before the magnetic barrier grows large.

In summary, we have made the first direct measurement of magnetic cavitation driven by heat flow rather than by bulk motion in the plasma. This magnetic cavitation is particularly relevant for experiments into magnetic reconnection—where rapid heating means that magnetic transport is often Nernst dominated—and for inertial confinement fusion, where applied or self-generated magnetic fields have been shown to increase temperatures in the hot spot and mitigate instability growth [18,39,40]. As described in Refs. [6,41], the expulsion of magnetic fields from the hottest regions of the plasma will increase the field strengths required for magnetized inertial confinement fusion techniques. We have shown that models without the Nernst term result in a spuriously high magnetic field within the plasma, and that under our moderately magnetized conditions XMHD models agree surprisingly well with kinetic simulations despite long mean free paths; the heat flow at the edge of the hot plasma remains relatively local due to the increase in the magnetic field outside the hot plasma.

The raw data and analysis code are available online; see Ref. [42]. Additional processed data is shown in Fig. 5, described in the appendix.

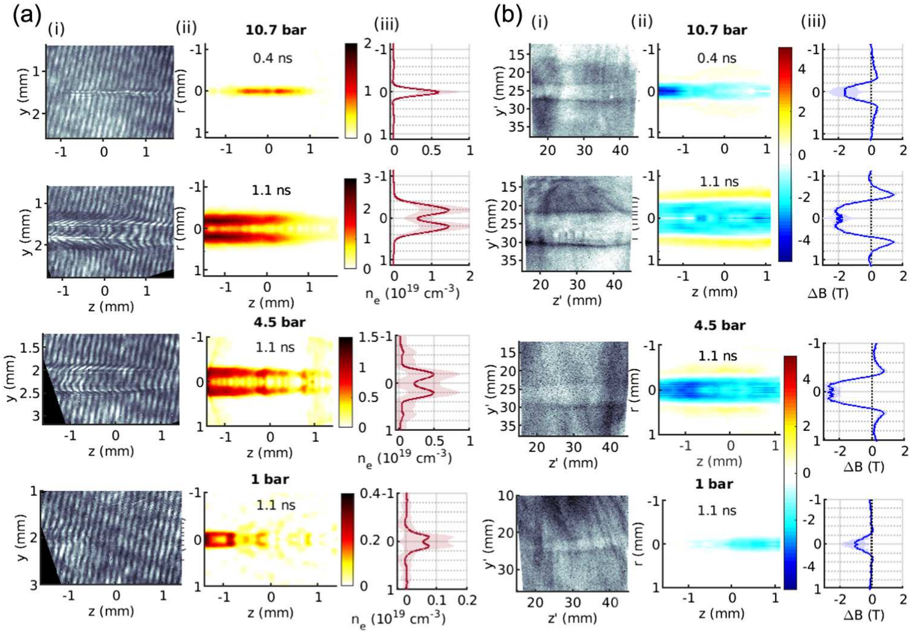

FIG. 5. (a) Interferometry results measured at gas jet backing pressures of 10.7 bar (top two rows), 4.5 bar (third row), and 1 bar (fourth row). Data at the highest backing pressure were taken at both 0.4 ns after the start of the heater beam (top panels) and 1.1 ns after (second row). (i) The raw interferogram measured on the camera is shown on the left, with fringe shifts showing the presence of a long plasma column. (ii) From this interferogram we reconstruct a map of the plasma density, shown as a cross section through the center of the column. (iii) The longitudinally averaged mean of the radial plasma density profile is shown to the right of this, with the shaded region showing the standard deviation longitudinally. (b) Radiography results measured at the same backing pressures and times. (i) The raw radiograph is shown on the left, with darker regions showing a higher proton dose. (ii) The change in the magnetic field reconstructed from the radiograph is shown as a cross section through the center of the plasma column, with (iii) the longitudinally averaged mean and standard deviation of the radial magnetic field profile to the right.

The authors are grateful for the support of LLNL Academic Partnerships (B618488), EUROfusion Enabling Research Grants No. AWP17-ENR-IFE-CCFE-01 and No. AWP17-ENR-IFE-CEA-02, and U.K. EPSRC Grants No. EP/P026796/1, No. EP/R029148/1, No. EP/M01102X/1, and No. EP/M011372/1. The authors particularly wish to thank the staff at Vulcan and Target Fabrication at the Central Laser Facility for all their support. Radiography calibration data from David Carroll and James Green were indispensable and we are grateful for IMPACT simulations conducted by Dominic Hill and advice with CTC from John Bissell. Part of this project was undertaken on the Viking Cluster, which is a high performance compute facility provided by the University of York. We are grateful for computational support from the University of York High Performance Computing service, Viking and the Research Computing team.

The experiment was designed by N. W., C. P. R., and M. P. R. and planned by C. A., P. B., G. S. H., O. C. E., L. A., Z. N., and N. W. The target area operators were G. S. H. and P. B., and M. N. was the facility link scientist. C. A. led the proton radiography setup, S. A. and G. S. H. were responsible for the pulsed power magnet, O. C. E. designed and built the optical probe layout, and K. G. built the system used for timing. P. B., L. A., and M. K. worked on all aspects of the experiment. A. D. and C. A. W. conducted fluid simulations, and A. D., C. A., and C. P. R. conducted VFP simulations with a code originally written by R. J. K.. C. A. conducted the radiography and interferometry analysis with P. B. and led the composition of the manuscript, with contributions and revisions from P. B., G. S. H., O. C. E., R. J. K., Z. N., C. P. R., and N. W.

Appendix: Additional data taken over a range of backing pressures.—These data show the raw interferograms and proton radiographs, the recovered density and magnetic field maps, and the longitudinally averaged density and magnetic field profiles. In the experimental campaign four shots were taken with both plasma and an applied magnetic field present. For completeness we show all of these data below, in Fig. 5, including the data previously shown in Fig. 2. At lower gas jet backing pressures, less heat is supplied to the plasma and the column of plasma is smaller and colder. The resulting magnetic cavitation is both smaller and weaker. Longitudinal averaged profiles from these data were used in Fig. 4.

---

[*] christopher.arran@york.ac.uk

[†] Present address: Centre Lasers Intenses et Applications, Université de Bordeaux-CNRS-CEA, 351 Cours de la Liberation, 33405 Talence, France.

[‡] Present address: Key Laboratory for Laser Plasmas (MoE) and School of Physics and Astronomy, Shanghai Jiao Tong University, 800 Dongchuan Road, 200240 Shanghai, China.

[1] L. Biermann, Z. Naturforsch. Teil A **5**, 65 (1950).
[2] S. I. Braginskii, J. Exp. Theor. Phys. **6**, 358 (1958).
[3] M. G. Haines, Plasma Phys. Controlled Fusion **28**, 1705 (1986).
[4] A. B. Sefkow, S. A. Slutz, J. M. Koning, M. M. Marinak, K. J. Peterson, D. B. Sinars, and R. A. Vesey, Phys. Plasmas **21**, 072711 (2014).
[5] J. R. Davies, R. Betti, P.-Y. Chang, and G. Fiksel, Phys. Plasmas **22**, 112703 (2015).
[6] S. A. Slutz, M. C. Herrmann, R. A. Vesey, A. B. Sefkow, D. B. Sinars, D. C. Rovang, K. J. Peterson, and M. E. Cuneo, Phys. Plasmas **17**, 056303 (2010).
[7] M. Hohenberger, P.-Y. Chang, G. Fiksel, J. P. Knauer, R. Betti, F. J. Marshall, D. D. Meyerhofer, F. H. Séguin, and R. D. Petrasso, Phys. Plasmas **19**, 056306 (2012).
[8] L. J. Perkins, D. D.-M. Ho, B. G. Logan, G. B. Zimmerman, M. A. Rhodes, D. J. Strozzi, D. T. Blackfield, and S. A. Hawkins, Phys. Plasmas **24**, 062708 (2017).
[9] J. D. Moody *et al.*, Phys. Rev. Lett. **129**, 195002 (2022).
[10] K. Behnia and H. Aubin, Rep. Prog. Phys. **79**, 046502 (2016).
[11] A. Nishiguchi, T. Yabe, M. G. Haines, M. Psimopoulos, and H. Takewaki, Phys. Rev. Lett. **53**, 262 (1984).
[12] L. Willingale *et al.*, Phys. Rev. Lett. **105**, 095001 (2010).
[13] C. Li *et al.*, Nucl. Fusion **53**, 073022 (2013).
[14] L. Lancia *et al.*, Phys. Rev. Lett. **113**, 235001 (2014).
[15] L. Gao, P. M. Nilson, I. V. Igumenshchev, M. G. Haines, D. H. Froula, R. Betti, and D. D. Meyerhofer, Phys. Rev. Lett. **114**, 215003 (2015).
[16] E. R. Tubman *et al.*, Nat. Commun. **12**, 334 (2021).
[17] G. Gregori, S. H. Glenzer, J. Knight, C. Niemann, D. Price, D. H. Froula, M. J. Edward, R. P. J. Town, A. Brantov, W. Rozmus, and V. Y. Bychenkov, Phys. Rev. Lett. **92**, 205006 (2004).
[18] D. H. Froula, J. S. Ross, B. B. Pollock, P. Davis, A. N. James, L. Divol, M. J. Edward, A. A. Offenberger, D. Price, R. P. J. Town, G. R. Tynan, and S. H. Glenzer, Phys. Rev. Lett. **98**, 135001 (2007).
[19] R. J. Henchen, M. Sherlock, W. Rozmus, J. Katz, D. Cao, J. P. Palastro, and D. H. Froula, Phys. Rev. Lett. **121**, 125001 (2018).
[20] C. P. Ridgers, R. J. Kingham, and A. G. R. Thomas, Phys. Rev. Lett. **100**, 075003 (2008).
[21] A. S. Joglekar, C. P. Ridgers, R. J. Kingham, and A. G. R. Thomas, Phys. Rev. E **93**, 043206 (2016).
[22] M. Borghesi, J. Fuchs, S. V. Bulanov, A. J. MacKinnon, P. K. Patel, and M. Roth, Fusion Sci. Technol. **49**, 412 (2006).
[23] See Supplemental Material at http://link.aps.org/supplemental/10.1103/PhysRevLett.131.015101 for additional details of the experimental setup, analysis, and simulations, which includes Refs. [24–31].
[24] R. A. Snavely *et al.*, Phys. Rev. Lett. **85**, 2945 (2000).
[25] S. C. Wilks, A. B. Langdon, T. E. Cowan, M. Roth, M. Singh, S. Hatchett, M. H. Key, D. Pennington, A. MacKinnon, and R. A. Snavely, Phys. Plasmas **8**, 542 (2001).
[26] W. H. Richardson, J. Opt. Soc. Am. **62**, 55 (1972).
[27] L. B. Lucy, Astron. J. **79**, 745 (1974).
[28] D. D. Hickstein, S. T. Gibson, R. Yurchak, D. D. Das, and M. Ryazanov, Rev. Sci. Instrum. **90**, 065115 (2019).

[29] E. W. Hansen and P.-L. Law, J. Opt. Soc. Am. A **2**, 510 (1985).

[30] E. Hansen, IEEE Trans. Acoust. Speech Signal Process. **33**, 666 (1985).

[31] M. Takeda, H. Ina, and S. Kobayashi, J. Opt. Soc. Am. **72**, 156 (1982).

[32] C. A. Walsh, J. P. Chittenden, D. W. Hill, and C. Ridgers, Phys. Plasmas **27**, 022103 (2020).

[33] N. L. Kugland, D. D. Ryutov, C. Plechaty, J. S. Ross, and H.-S. Park, Rev. Sci. Instrum. **83**, 101301 (2012).

[34] M. F. Kasim, A. F. A. Bott, P. Tzeferacos, D. Q. Lamb, G. Gregori, and S. M. Vinko, Phys. Rev. E **100**, 033208 (2019).

[35] C. Arran, C. P. Ridgers, and N. C. Woolsey, Matter Radiat. Extremes **6**, 046904 (2021).

[36] J. J. Bissell, C. P. Ridgers, and R. J. Kingham, Phys. Rev. Lett. **105**, 175001 (2010).

[37] R. J. Kingham and A. R. Bell, J. Comput. Phys. **194**, 1 (2004).

[38] M. Sherlock and J. J. Bissell, Phys. Rev. Lett. **124**, 055001 (2020).

[39] P. Y. Chang, G. Fiksel, M. Hohenberger, J. P. Knauer, R. Betti, F. J. Marshall, D. D. Meyerhofer, F. H. Séguin, and R. D. Petrasso, Phys. Rev. Lett. **107**, 035006 (2011).

[40] C. A. Walsh, K. McGlinchey, J. K. Tong, B. D. Appelbe, A. Crilly, M. F. Zhang, and J. P. Chittenden, Phys. Plasmas **26**, 022701 (2019).

[41] R. D. McBride and S. A. Slutz, Phys. Plasmas **22**, 052708 (2015).

[42] C. P. Ridgers and C. Arran, Data and analysis code for "Measurement of Magnetic Cavitation Driven by Heat Flow in a Plasma," available at 10.15124/bd949fdd-1c2c-4d04-b2eb-785065198a69, University of York (2021).